ACS APPLIED MATERIALS & INTERFACES

Research Article

www.acsami.org

Novel Slurry Electrolyte Containing Lithium Metasilicate for High Electrochemical Performance of a 5 V Cathode

Yonghuan Ren,[†,‡] Daobin Mu,[*,†] Feng Wu,[†] and Borong Wu[*,†]

[†]School of Materials Science and Engineering, Beijing Institute of Technology, Beijing 100081, China

[‡]Xiamen King Long United Automotive Industry Corporation, Limited, Xiamen 361023, China

ABSTRACT: We report a novel slurry electrolyte with ultrahigh concentration of insoluble inorganic lithium metasilicate (Li_2SiO_3) that is exploited for lithium ion batteries to combine the merits of solid and liquid electrolytes. The safety, conductivity, and anodic and storage stabilities of the eletrolyte are examined, which are all enhanced compared to a base carbonate electrolyte. The compatibility of the elecrolyte with a $LiNi_{0.5}Mn_{1.5}O_4$ cathode is evaluated under high voltage. A discharge capacity of 173.8 mAh g^{-1} is still maintained after 120 cycles, whereas it is only 74.9 mAh g^{-1} in the base electrolyte. Additionally, the rate capability of the $LiNi_{0.5}Mn_{1.5}O_4$ cathode is also improved with reduced electrode polarization. TEM measurements indicate that the electrode interface is modified by Li_2SiO_3 with a thinner solid electrolyte interphase film. Density functional theory computations demonstrate that $LiPF_6$ is stabilized against its decomposition by Li_2SiO_3. A possible path for the reaction between PF_5 and Li_2SiO_3 is also proposed by deducing the transition states involved in the process using the DFT method.

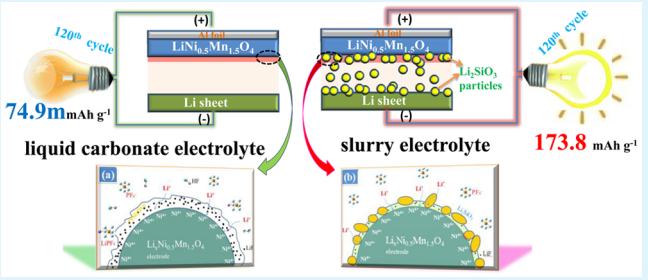

KEYWORDS: *slurry electrolyte, lithium metasilicate, high voltage, cycling stability, ultrahigh concentration*

1. INTRODUCTION

Currently, with ground transportation moving toward electrification, i.e, replacing vehicles driven by internal combustion engines (ICE) with electric-driven ones, brings about great challenges to secondary batteries.[1,2] Lithium ion batteries (LIBs) offer many advantages based on their high energy density and long life; they are a success of modern technology that realizes energy conversion. However, it is indispensable to enhance their performance further for an increasing variety of applications, in particular, their use in electric vehicles (EV), which demand a higher energy density of the battery to promote endurance. The energy density is basically defined as the product of the specific capacity and operating voltage. Increasing the working potential of the cathode, in addition to enhancing the capacity, is also currently underway. However, it confronts formidable problems associated with the deterioration of cell performance on cycle stability and safety.[3] Material modifications have been given much attention for high voltage cathodes in which structure change commonly occurs during cycling. In addition, with the instability of the state-of-art electrolyte under high voltage, the demand for electrolytes with high anodic stability grows drastically to match the development of high voltage cathodes.

As a successful high voltage cathode material,[4] the specific capacity of spinel structure $LiNi_{0.5}Mn_{1.5}O_4$ (LNMO) can reach as high as 260 mAh g^{-1} within 2.0−5.0 V, where both 8a tetrahedral sites and 16c octahedral sites are responsible for lithium ion insertion/extraction.[5,6] Its energy density is ∼900 Wh kg^{-1} using a lithium sheet as a counter electrode. Unfortunately, the cycling stability of the $LiNi_{0.5}Mn_{1.5}O_4$ cathode is not satisfactory in a wide voltage range, especially at high rates,[7] because oxygen is evolved and the carbonate electrolyte decomposes around 5.0 V versus Li^+/Li.[8] Despite many studies on material modifications,[9−11] currently, only a few studies have focused on electrolytes that can improve the interface compatibility of the electrode cycled in the range of 2.0−5.0 V.

Ionic liquid, gel, and solid electrolytes seem to be potential candidates for high voltage batteries due to their high electrochemical stability and safety. However, the low Li^+ conductivity and poor electrode/electrolyte compatibility limit wider applications. Liquid electrolyte still plays a key role in commercial lithium-ion batteries to allow fast migration of lithium ions between the cathode and anode. It also provides a sufficient surface-to-surface wetting effect, not like the point-to-point contact in a solid electrolyte.[12] The electrolyte additives are usually used to attain the enhancement in electrochemical properties or safety of LIB. Traditionally, they are soluble in liquid electrolyte and added at less than 5%. In this work, to combine the merits of solid and liquid electrolytes, insoluble inorganic particles of lithium metasilicate (Li_2SiO_3) in a large amount are mixed with carbonate electrolyte to make a slurry electrolyte, taking advantage of the superior compatibility of the solid phase Li_2SiO_3 in LIB.[13] The electrolyte properties on

Received: June 28, 2015
Accepted: September 25, 2015
Published: September 25, 2015

DOI: 10.1021/acsami.5b05780
ACS Appl. Mater. Interfaces 2015, 7, 22898−22906

safety, conductivity, and anodic and storage stabilities are studied, and its compatibility with a 5 V $LiNi_{0.5}Mn_{1.5}O_4$ cathode is investigated under high voltage using a base carbonate electrolyte as comparison.

2. EXPERIMENTAL SECTION

2.1. Preparation of Electrolyte, Electrode, and Cells. At a weight ratio of 30:100, Li_2SiO_3 (99.9%, Aladdin Chemistry Co. Ltd., China, 0.2−1 μm in diameter) and carbonate electrolyte (1 mol L^{-1} lithium hexafluorophosphate ($LiPF_6$)-ethylene carbonate (EC)/propylene carbonate (PC)/diethyl carbonate (DEC) (1:1:3 wt, base electrolyte) were mixed in a plastic bottle in an Ar-filled glovebox and vibrated to make a slurry electrolyte denoted as ESS-30. The solvents and $LiPF_6$ were obtained from Xianghe Kunlun Chemical Products Co., Ltd., China. $LiNi_{0.5}Mn_{1.5}O_4$ (obtained from the Institute of Nuclear & New Energy Technology, Tsinghua University, China) mixed with 10 wt % super P and 10 wt % polyvinylidene fluoride (PVDF, dissolved in 1-methyl-2-pyrrolidinone) were used to make the cathode disk. CR2025 coin cells were assembled in the Ar-filled glovebox with Celgard 2400 polyethylene membrane as a separator. The cells were left for 24 h prior to cycling from 2.0 to 5.0 V on a CT2001A Land tester (Wuhan Jinnuo Electronics Co., Ltd.).

2.2. Characterization and Electrochemical Measurements. Linear sweep voltammetry (LSV), cyclic voltammetry (CV), and electrochemical impedance spectroscopy (EIS) tests (1 Hz to 0.1 MHz, 5 mV perturbation) were performed on a CHI660c electrochemical station (Shanghai Chenhua Co. Ltd.). For the measurements of self-extinguishing time (SET), glass fiber (0.05−0.06 g) adsorbing ~0.55 g electrolyte was ignited by matchstick in a wind-free room with dry air and low humidity. The burning time was recorded using a timer. Six parallel samples were measured to ensure reproducibility and obtain an average SET value of each electrolyte.

Conductivity was tested using the ac impedance method, and the transference number (t_+) for the electrolytes was evaluated according to a direct-current polarization measurement using eq 1.

$$t_+ = \frac{I^s(\Delta V - I^0 R_{el}{}^0)}{I^0(\Delta V - I^s R_{el}{}^s)} \quad (1)$$

In eq 1, the subscripts '0' and 's' indicate initial and steady-state values, respectively. R_{el} is the electrode resistance containing the passive film resistance (R_{film}) and the charge transfer resistance (R_{ct}), ΔV is the applied voltage, and I is the steady current in the chronoamperometric curves. A two-electrode symmetric cell was used in the t_+ measurement,[14] where two lithium sheets (1.89 cm^2 area) sandwiched a Celgard (2400) porous polypropylene separator. A constant dc bias (30 mV) was applied to the cell, and the steady-state current (I_s) was obtained with the chronoamperometric curves after a pulse width of 150 s.

Surface analysis was carried out by a JEM-2100 high resolution transmission electron microscope (HRTEM). ^{13}C nuclear magnetic resonance (NMR) spectroscopy of the electrolytes was measured on a Varian mercury-plus 400 spectrometer with deuterated chloroform ($CDCl_3$) as the internal reference.

2.3. Computational Details. Theoretical calculations were performed based on the Gaussian 09 program. The method used was density functional theory (DFT) with Becke's three parameters (B3) exchange functional along with the Lee−Yang−Parr (LYP) nonlocal correlation functional (B3LYP). All of the complexes (including equilibrium and transition state structures) were treated at B3LYP/6-31+G(d,p) level for full geometry optimization and natural bond orbital (NBO) analysis. The dielectric constant was set at 27.47 for geometry optimization in solvent phase, which was calculated from the EC/PC/DEC(1/1/3) system. Frequency analyses were done with the same basis set to deduce the transition states and make zero-point energy (ZPE) corrections. For confirmation of whether the transition state correctly connected the reactants and products under consideration, intrinsic reaction coordinate (IRC) calculations were also performed. Gibbs free energies of optimized reactants, products, and transition states were calculated on the basis set of B3LYP/6-311++G(d,p) level.

3. RESULTS AND DISCUSSION

3.1. Properties of the Slurry Electrolyte. *a. Flammability.* Liquid electrolytes easily suffer from high flammability, resulting in severe safety issues in their application. Great effort has been paid to suppress fires through the addition of fire retardant additives or replacing the liquid electrolyte with an ionic liquid. In this work, it is expected that the substitution of noncombustible salt for the applied liquid electrolyte could also improve the safety with a decrease in the combustible carbonate solvents. Figure 1 displays the self-extinguishing time (SET) of

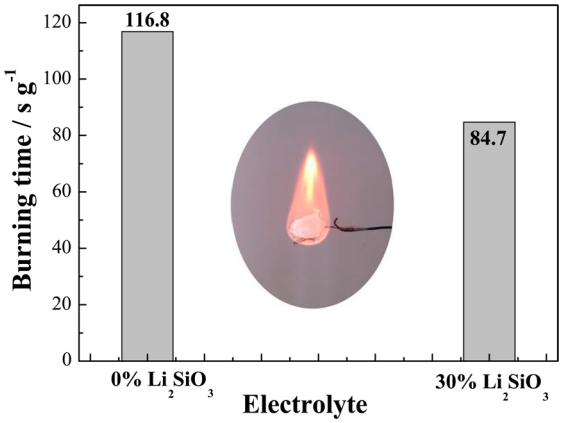

Figure 1. Self-extinguishing time of $LiPF_6$-EC/PC/DEC electrolyte containing different content of Li_2SiO_3 (30% mentioned in this paper stands for the weight ratio of Li_2SiO_3 to the base electrolyte), and the inset is a picture of the electrolyte burning on a glass fiber.

the electrolytes. The SET value of the base electrolyte is 116.8 s g^{-1}. As expected, the SET of ESS-30 decreases to 84.7 s g^{-1}. The self-extinguishing property of the slurry electrolyte is shown to be superior to that of the base electrolyte. Replacing part of carbonate electrolyte by Li_2SiO_3 slows some of the danger of combustion. Hence, the ESS-30 is beneficial towards the safety of lithium ion batteries.

b. Conductivity. As shown in Figure 2(a), the diameter of the semicircle for the case of a Li/Li cell with ESS-30, which corresponds to R_{el}, is one order magnitude smaller than with the base sample. Meanwhile, its steady state current (at 150 s) displayed in Figure 2(b) is 13 times larger than that of the base one. The transference number of Li^+ (t_{Li+}) was calculated by the method of Bruce and Vincent[15−17] according to the results in Figure 2(a) and (b). The calculated t_{Li+} is 0.19 and 0.42 for the base electrolyte and the ESS-30 (Figure 2(c)), respectively, meaning it is enhanced in the presence of Li_2SiO_3. Figure 2(d) displays the conductivities of the electrolytes ($\kappa_{electrolyte}$) at various temperatures. The values are slightly lower for ESS-30 compared to the ones of the base electrolyte. For example, under −40 °C, the $\kappa_{electrolyte}$ of ESS-30 is shown to be 0.44 × 10^{-3} S cm^{-1}, which is 14% smaller than 0.50 × 10^{-3} S cm^{-1} of the base electrolyte. However, its $\kappa_{electrolyte}$ is still higher than 1.35 × 10^{-3} S cm^{-1} at the temperature above −20 °C, comparatively superior to the ones of ionic liquid, gel, or solid electrolytes despite the lower liquidity of the slurry electrolyte. Combining the results in Figure 2(c) and (d), the conductivity of Li^+ (κ_{Li+}) was estimated in terms of $\kappa_{Li+} = \kappa_{electrolyte} \times t_{Li}{}^+$; κ_{Li+} at 20 °C appears to be facilitated from 1.58 mS cm^{-1} of the

DOI: 10.1021/acsami.5b05780
ACS Appl. Mater. Interfaces 2015, 7, 22898−22906

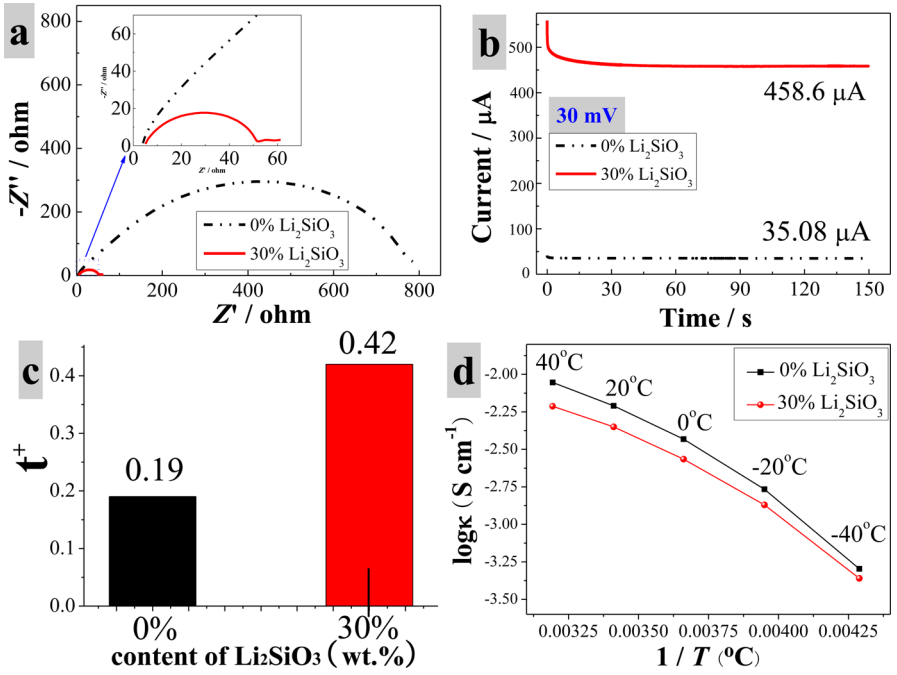

Figure 2. Properties of electrolytes. (a) EIS impedance spectra for the Li/Li cells after being measured in the chronoamperometry experiment. (b) Chronoamperometric curves with a constant dc bias (30 mV). (c) Transference number of Li^+. (d) Electrolyte conductivity.

base electrolyte to 2.14 mS cm^{-1} of ESS-30. The κ_{Li+} is critical for electrolyte performance because the charges used for lithation/delithiation are mainly carried by lithium ions. Thus, the ultrahigh concentrated Li_2SiO_3 particles do not hinder the mobility of Li^+. In contrast, they improve the conductivity of Li^+. The reason for this will be explored later.

c. Anodic Stability. Figure 3 shows the LSV curves obtained on a Pt electrode in the two electrolytes. Oxidation current

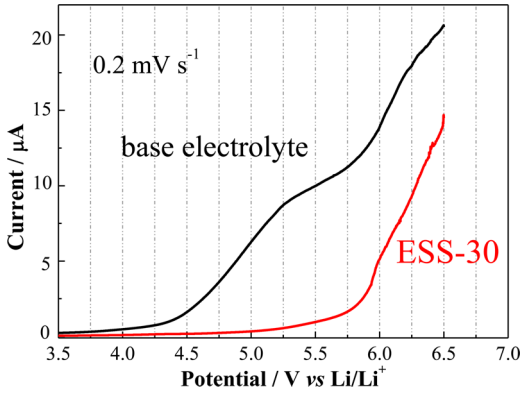

Figure 3. LSV curves of the base and ESS-30 electrolytes on a Pt electrode.

starts increasing intensely from the potential above 4.5 V for the base electrolyte, meaning large amounts of electrolyte are oxidized on the Pt electrode. However, the reaction is suppressed in the case of ESS-30, and no obvious oxidation current is detectable until the potential increases up to 5.5 V. The side reactions aroused by impurities in electrolyte may be retarded in the presence of Li_2SiO_3 such that the anodic stability of the slurry electrolyte is improved. Assumably, the superior electrochemical stability may be helpful for the performance enhancement of the cathode cycled under high voltage.

d. Electrolyte Storage Stability. The ultrahigh concentration of Li_2SiO_3 makes the electrolyte like a slurry with low liquidity, as seen in Figure 4(a). It is obviously different from the

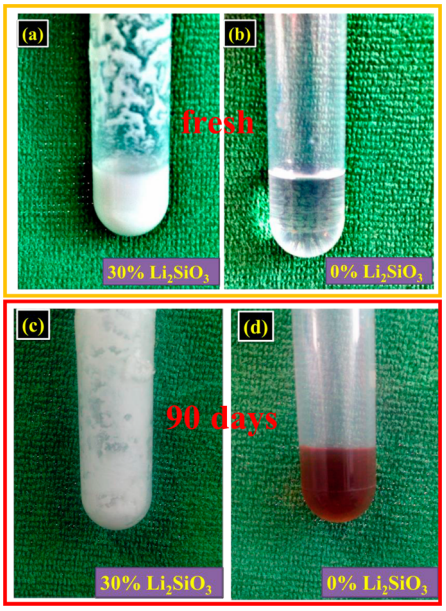

Figure 4. Pictures of fresh electrolytes (a, 30% Li_2SiO_3; b, 0% Li_2SiO_3) and stored electrolytes after 90 days (c, 30% Li_2SiO_3; d, 0% Li_2SiO_3).

transparent liquid in Figure 4(b). After being stored in a sealed centrifuge tube for 90 days in the laboratory at room temperature, the transparent electrolyte becomes brown. Moisture measurements show that the water content in the base electrolyte increases from 35.2 to 153.7 ppm after 90 days. The high moisture could accelerate the hydrolysis decomposition of $LiPF_6$ to produce HF and PF_5 ($LiPF_6 \rightarrow LiF + PF_5$, $PF_5 + H_2O \rightarrow POF_3 + 2HF$). As determined by acidity

DOI: 10.1021/acsami.5b05780
ACS Appl. Mater. Interfaces 2015, 7, 22898−22906

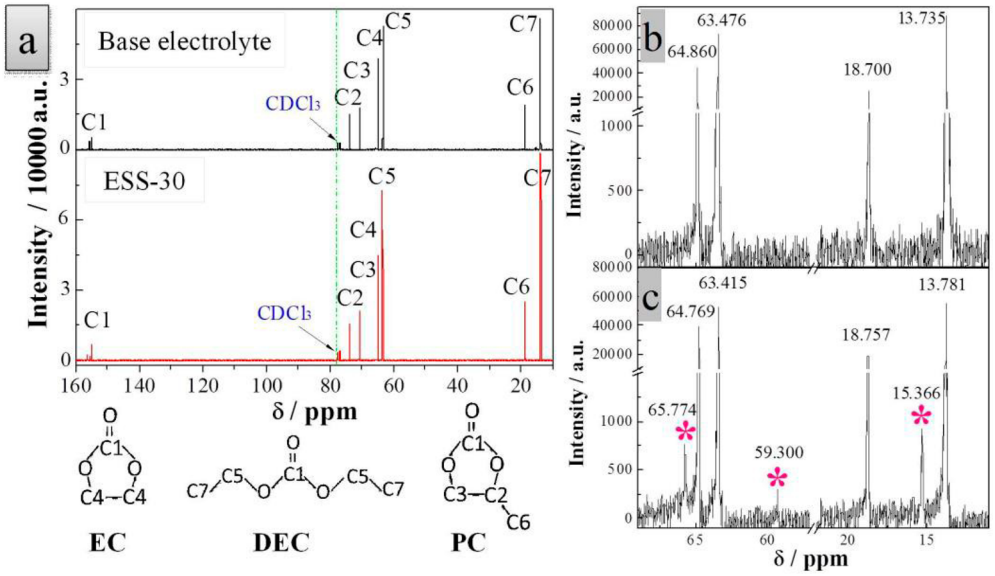

Figure 5. (a) ^{13}C NMR spectra of two electrolytes after storage; (b, c) the enlarged spectra for the ESS-30 (b) and base electrolyte (c).

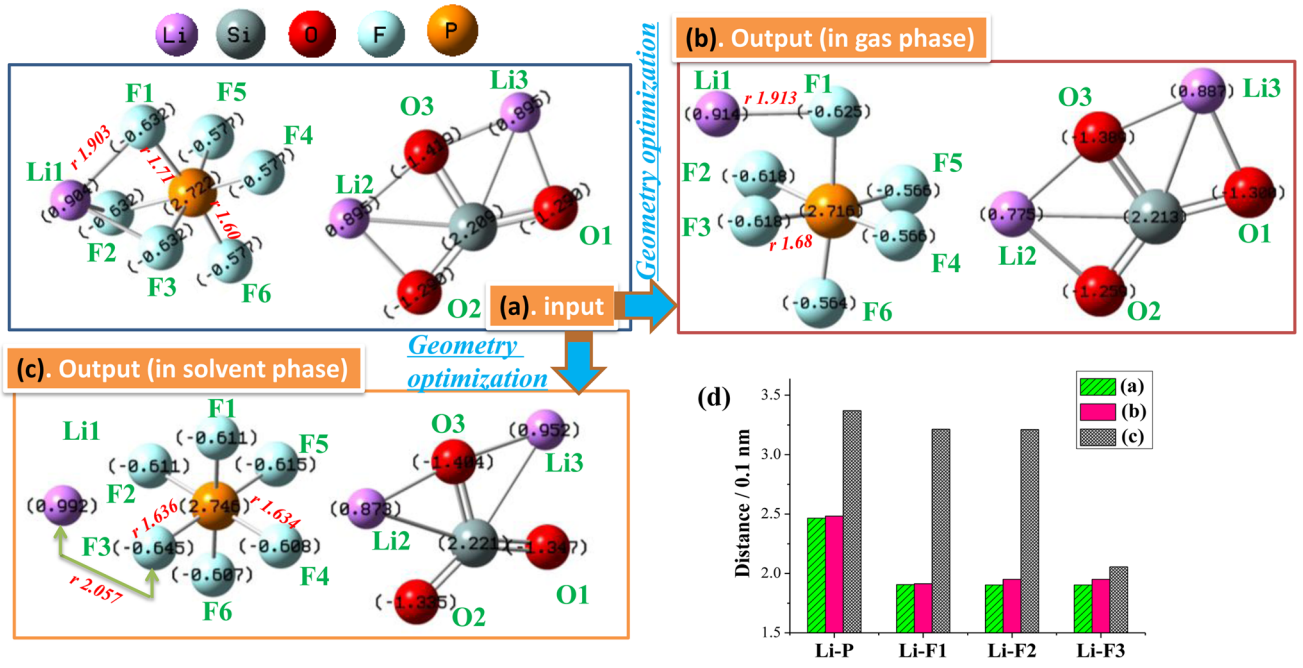

Figure 6. Schematic representation of the effect of Li_2SiO_3 on $LiPF_6$ dissociation. (a) Original structures of Li_2SiO_3 and $LiPF_6$ molecules as input file; (b, c) optimized results for $LiPF_6$ in the presence of Li_2SiO_3 in gas (b) and solvent (c) phases. (d) The distances between Li1 and P, F1, F2, F3 atoms for $LiPF_6$ in (a), (b), and (c).

measurements, the content of HF does increase from 145.9 to 2474.65 ppm after 90 days. It is harmful to Mn-based cathodes because HF can accelerate Mn dissolution.[18] In addition, the generated PF_5 may initiate the polymerization of cyclic carbonates due to its high reactivity,[19,20] turning the electrolyte a brown color. With the special appearance of ESS-30, the contents of H_2O and HF are difficult to test by the same method used in the base electrolyte. However, it is clear that the ESS-30 displays a negligible color change after the storage (this also happens when stored at 60 °C). It is thought that the solvent polymerization causing the color change has been suppressed. The speculation is then confirmed by ^{13}C NMR measurements. As shown in Figure 5a, C1−C7 carbon peaks are detected. They can be attributed to EC, PC, DEC (the three peaks at 154−156 ppm represent $-OCO_2-$ of the three carbonates, which are all called C1 for simplicity). In the case of the base electrolyte, impurity peaks at 65.774, 59.300, and 15.366 ppm appear as seen in Figure 5c, which should originate from the polymeric products of carbonate solvents. However, none of the impurity carbon peaks are detected for the ESS-30 sample, as shown in Figure 5b. Thus, it is inferred that no carbonate polymerization occurs during the storage over 90 days. This may be ascribed to two reasons: (1) $LiPF_6$ decomposition producing PF_5 is inhibited and (2) the generated PF_5 is consumed. DFT computations were employed to further elucidate the mechanism.

The intrinsic structures of the Li_2SiO_3 and $LiPF_6$ molecules are shown in Figure 6(a). Panels b and c in Figure 6 are the

DOI: 10.1021/acsami.5b05780
ACS Appl. Mater. Interfaces 2015, 7, 22898−22906

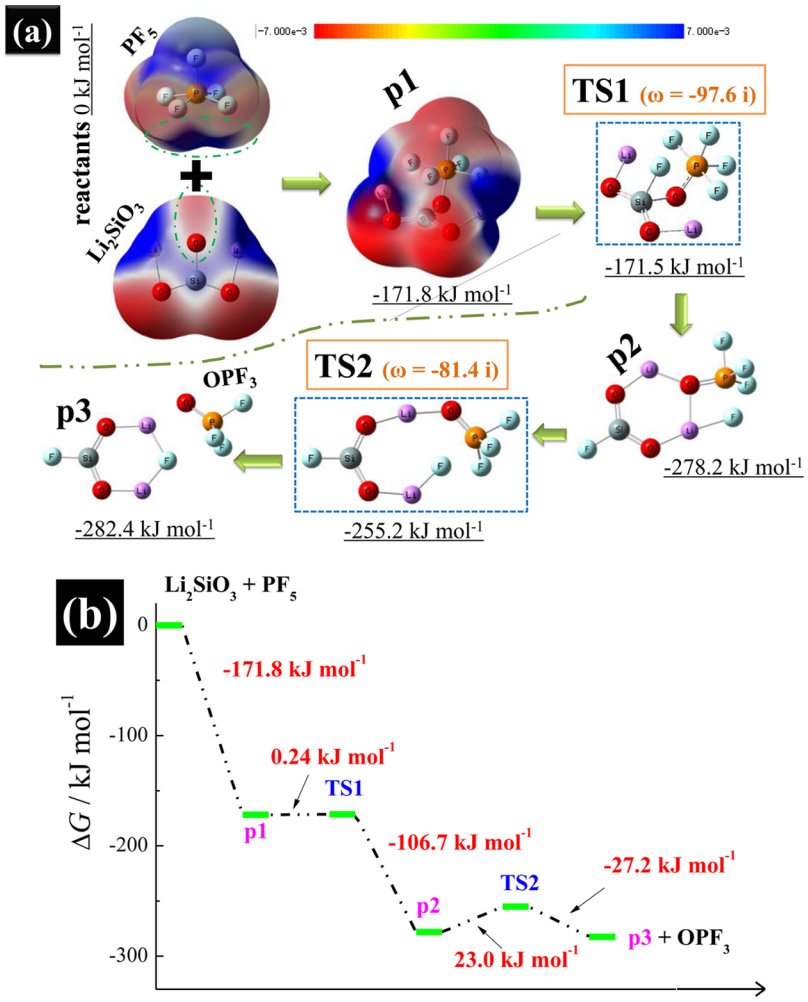

Figure 7. Geometry optimization (a) and potential energy profile (b) of the complexes generated during the process of the reaction between Li_2SiO_3 and PF_5.

geometry optimization results of the $LiPF_6$ structure in the presence of Li_2SiO_3 in gas and solvent phases, respectively. As conducted in gas phase, Li1 connects with PF_6 through only one F atom (F1), no longer through F2 and F3 atoms as ever. The distances between Li1 and P, F1, F2, F3 atoms all increase slightly, as shown in Figure 6(d). This means that the binding energy for the Li1 connection to PF_6 is weakened, which will be helpful for $LiPF_6$ dissociation. In the solvent phase, Figure 6(c) shows that the Li1 cation of $LiPF_6$ no longer even bonds with any F atom in the presence of Li_2SiO_3. The distance between the Li1 cation and the nearest F atoms (F2) in the PF_6 complex becomes 2.057 Å, which is larger than the original value of 1.90 Å in $LiPF_6$. The bond lengths of P−F(1−6) decrease; P−F3, for example, shortens from 1.71 to 1.64 Å. All the bond lengths of P−F(1−6) almost turn out to be equal, presenting more stable PF_6^-. The two results in gas and solvent phases both reflect that the distances between Li and F atoms of $LiPF_6$ are extended by Li_2SiO_3. This may be caused by the stronger electronegativity of SiO_3^{2-} than PF_6^-, which makes Li2 and Li3 more electrophilic than Li1 to attract PF_6^-. Then, the interactions between Li1 and F(1, 2, 3) in $LiPF_6$ are weakened, which is helpful for the dissociation of $LiPF_6$ and retarding the $LiPF_6$ decomposition producing LiF and PF_5.[18] It is well-known that $LiPF_6$ decomposition can reduce the number of free Li ions available for charge transportation and also seriously deteriorate the performance of the electrolyte in many respects.[21] Here, the $LiPF_6^-$—electrolyte is stabilized with weakened decomposition by Li_2SiO_3, such that superior storage stability is attained with no color change, and an adequate number of free Li ions can be guaranteed. In addition, because the dissociation of $LiPF_6$ is promoted in ESS-30, more free Li^+ are generated, which are also responsible for the increased t^+ and κ_{Li+} phenomenon seen in Figure 2(c).

Furthermore, provided that the generated PF_5 is consumed by Li_2SiO_3, then what is the reaction path between them? First, electronic static potential (ESP) is utilized to illustrate the electronegativity of the two molecules. Figure 7(a) shows the ESP mapped on the isosurface of the electronic density of each molecule. In the contour map, the red and blue colors represent the most electronegative and electropositive ESP values, respectively. Very negative electrostatic potential is displayed surrounding the oxygen atoms of Li_2SiO_3, and very positive values are shown at both the top and the bottom of PF_5. An electrostatic interaction takes place between the blue and red regions marked with elliptical dashed lines, leading to product 1 (denoted as p1) in an equilibrium state with a Gibbs change of −171.8 kJ mol^{-1} (assuming the Gibbs free energy of the reactants is 0 kJ mol^{-1}). Sequentially, it proceeds via a transition state (TS1, −171.5 kJ mol^{-1}) to bring about p2 (−278.2 kJ mol^{-1}); the ΔG for (p1 → p2) is −106.46 kJ mol^{-1}.

DOI: 10.1021/acsami.5b05780
ACS Appl. Mater. Interfaces 2015, 7, 22898−22906

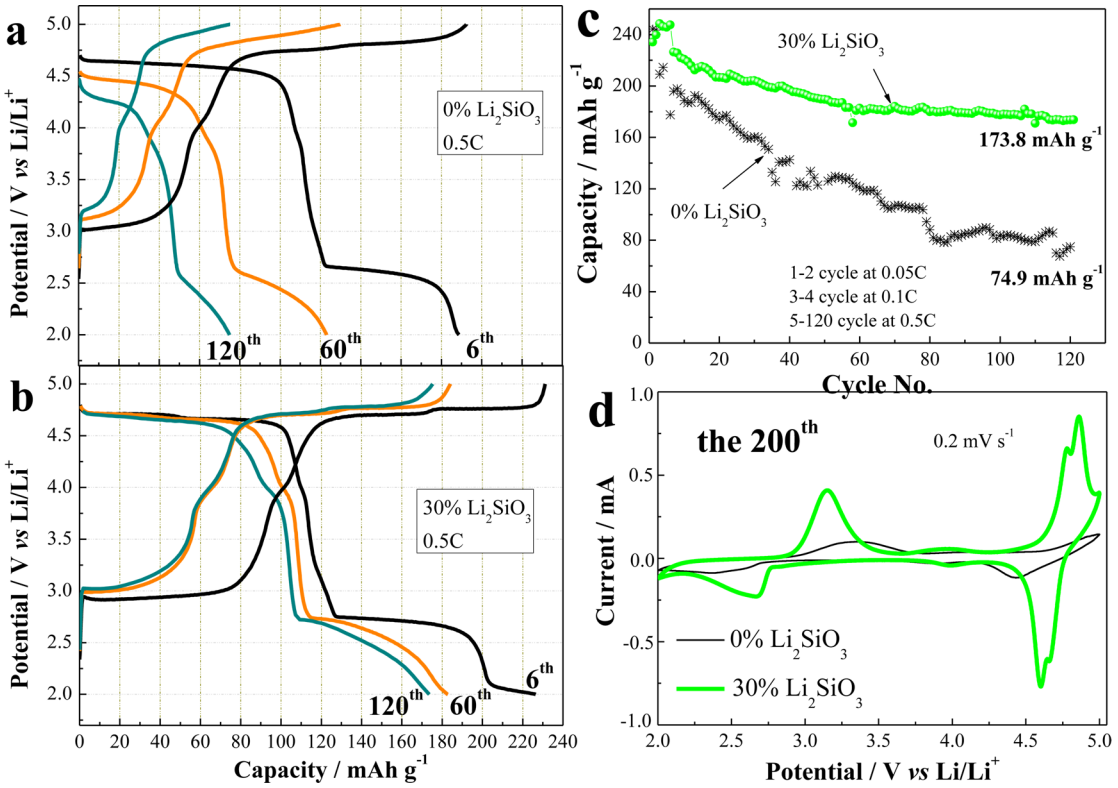

Figure 8. (a, b) Potential profiles of the LNMO cathode after various cycles, (c) the discharge capacity with cycling, and (d) CV curves of the LNMO cathode at the 200th cycle in the two electrolytes (0.1 C = 25 mA g^{-1}).

According to frequency analysis, TS1 has only one imaginary frequency (ω) at −97.6 cm^{-1} with vibration orientations linked to p1 and p2. Then, the process further goes through TS2 (−255.2 kJ mol^{-1}), producing p3 and OPF_3 (−282.4 kJ mol^{-1} in total) with a ΔG of −4.2 kJ mol^{-1}. Also, only one imaginary frequency appears for TS2 at −81.4 cm^{-1} with the vibration orientations pointed to p2 and p3 + OPF_3. So far, $Li_2SiO_2F_2$ (*p3*) and OPF_3 are produced, and the potential energy profile can be seen in Figure 7(b). However, p3 is thought to further react with HF to finally bring into being Li_2SiF_6, which is detected in the $LiPF_6$/PC + Li_2SiO_3 solution in our previous work[13] (following $Li_2SiO_2F_2 + 4HF \rightarrow Li_2SiF_6 + 2H_2O$). As calculated, the ΔG of the reaction is −261.0 kJ mol^{-1}, further supporting the above hypothesis.

According to reactions 3 and 4, reaction 5 could be obtained. Binding reactions 2 and 5, the total reaction is $Li_2SiO_3 + 3PF_5 \rightarrow 3OPF_3 + Li_2SiF_6$, i.e., Li_2SiO_3 can react with PF_5 without producing HF or H_2O but giving Li_2SiF_6. As PF_5 is consumed, the HF generated from reaction 2 could also then be retarded.

$$LiPF_6 \rightarrow LiF + PF_5 \quad (1)$$

$$PF_5 + H_2O \rightarrow OPF_3 + 2HF \quad (2)$$

$$Li_2SiO_3 + PF_5 \rightarrow Li_2SiO_2F_2 + OPF_3 \quad (3)$$

$$Li_2SiO_2F_2 + 4HF \rightarrow Li_2SiF_6 + 2H_2O \quad (4)$$

$$Li_2SiO_3 + 6HF \rightarrow Li_2SiF_6 + 3H_2O \quad (5)$$

$$(2) + (5): Li_2SiO_3 + 3PF_5 \rightarrow 3OPF_3 + Li_2SiF_6 \quad (6)$$

3.2. Electrochemical Performance. The compatibility of this slurry electrolyte with LNMO cathode is evaluated in the potential range of 2.0−5.0 V.[5,22,23,25] Plateaus around 4.7 and 2.7 V in Figure 8(a) and (b) correspond to the redox peaks of Ni^{2+}/Ni^{4+} and Mn^{3+}/Mn^{4+}, respectively. However, in the case with the base electrolyte, almost no plateau appears after 120 cycles, and the voltage drops rapidly, as shown in Figure 8a. In contrast, with ESS-30, the curve at the 120th cycle similarly follows the shape at the sixth cycle with only a slight voltage difference. Figure 8(c) displays the variation of capacity relative to cycle number. A charge/discharge capacity of 175.3/173.8 mAh g^{-1} is still maintained after 120 cycles in the case with ESS-30, whereas it is 75.2/74.9 mAh g^{-1} for the base electrolyte sample. It is worth noting that in the voltage range of 3.5−5.0 V, which is more applicable, the discharge capacity is also much higher for the former at 103 relative to 44 mAh g^{-1}. It has been suggested that the spinel material suffers capacity fading because of Mn dissolution, intensive electrolyte reaction above 4.9 V, and Jahn−Teller distortion around 3 V due to the existence of high spin Mn^{3+}.[24] In the presence of Li_2SiO_3, Mn dissolution might be suppressed because HF generation is inhibited, and electrolyte oxidation under high voltage is also reduced with the superior anodic stability of the slurry electrolyte. Hence, the capacity decay is mitigated. The CV curves in Figure 8(d) reflect severe sluggish kinetics of the electrode in the base electrolyte after 200 cycles. The two pairs of redox peaks around 4.7 and 2.7 V become broadened with low current intensities, and the redox peak potential difference increases. On the contrary, stronger peaks with higher current intensities can still be observed after 200 cycles in the case of ESS-30; the two pairs of splitting peaks around 4.7 V ascribed to Ni^{2+}/Ni^{3+} and Ni^{3+}/Ni^{4+} redox couples are maintained as well. The behavior indicates superior cycling stability, reversibility, and activity of the cathode in the ESS-30 even after 200 cycles.

DOI: 10.1021/acsami.5b05780
ACS Appl. Mater. Interfaces 2015, 7, 22898−22906

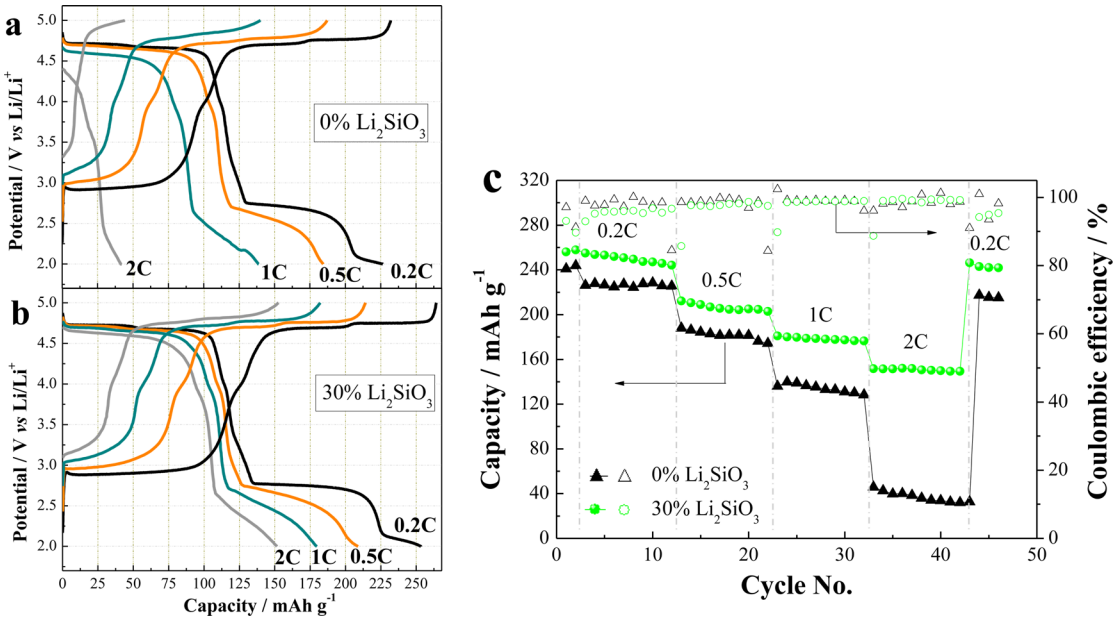

Figure 9. (a, b) Potential profiles of a LNMO cathode at various rates and (c) the discharge capacity and Coulombic efficiency with cycling at different rates in the two electrolytes (1 C = 250 mA g^{-1}).

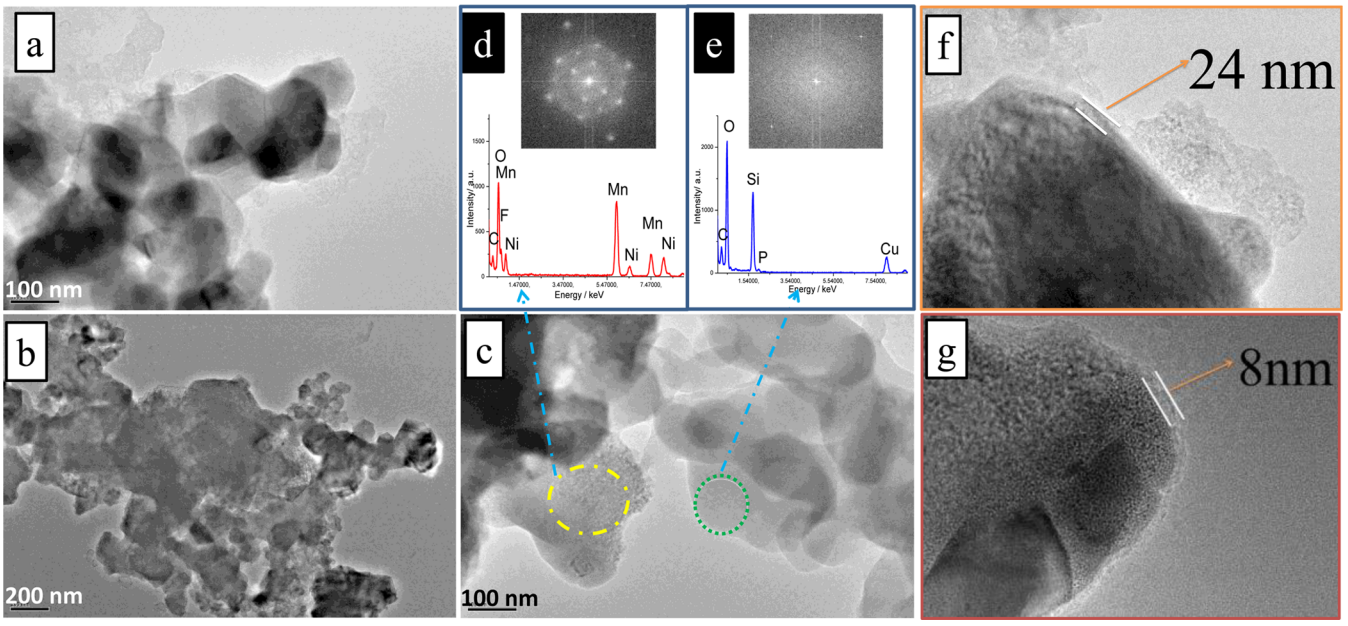

Figure 10. TEM images of the LNMO electrode after 120 cycles in the base (a, f) and ESS-30 (b, c, g) electrolytes, and the EDX and electron diffraction patterns for the substances in different regions.

The rate performance of the LNMO cathode cycled in the two electrolytes is shown in Figure 9. The discharge capacities of 226.5 and 253.2 mAh g^{-1} are delivered at 0.2 C for the cathodes in the base electrolyte and ESS-30, respectively. However, a dramatical decline of discharge potential is displayed at 2 C in the case with the base electrolyte, where only 42.5 mAh g^{-1} can be delivered (Figure 9a). However, with ESS-30, the discharge plateaus are still visible at 2 C as seen in Figure 9(b). The potential difference between the two cases at 2 and 0.2 C is obviously smaller than that of the base electrolyte. The capacities of 264.2/253.2, 214.1/208.9, and 182.1/179.7 mAh g^{-1} are charged/discharged at current rates of 0.2, 0.5, and 1 C, respectively. Even at 2 C, the charge capacity of 152.7 mAh g^{-1} can be obtained, and the discharge capacity up to 151.5 mAh g^{-1} is delivered within ~19 min, which is almost 2.5 times larger than the one with the base electrolyte. Moreover, when the current rate returns to 0.2 C, a reversible discharge capacity of 241.8 mAh g^{-1} is again obtained, remaining at 95% of its initial capacity at 0.2 C. However, the capacity only recovers to 215.0 mAh g^{-1} with the base electrolyte. The improvement of the rate performance is thought to be attributed to the relief of electrode polarization because side reactions between the electrolyte and delithiated cathode may be inhibited in the presence of Li_2SiO_3, which weakens the aggregation of the decomposition products on the cathode surface, decreasing the resistance of lithiation/delithiation.[13] It is now clear that the large amount of substitution of carbonate electrolytes by insouble material

DOI: 10.1021/acsami.5b05780
ACS Appl. Mater. Interfaces 2015, 7, 22898−22906

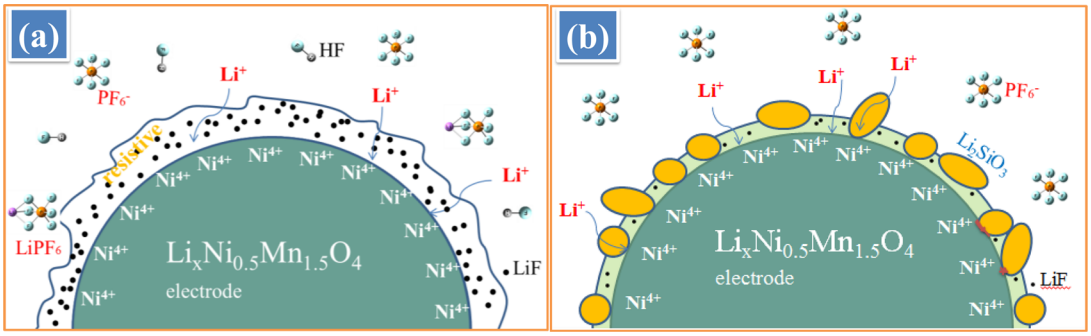

Figure 11. Scenario of the electrolyte/cathode interface with (a) the base electrolyte and (b) the slurry electrolyte.

(Li_2SiO_3) indeed enhances the electrochemical performance of the LNMO cathode without introducing damage. Good compatibility is confirmed between the slurry electrolyte and LNMO cathode within 2.0−5.0 V.

Figure 10 shows the TEM images of the electrode after 120 cycles. In the case of the base electrolyte, only one phase appears in Figure 10a besides Super P, representing LNMO material. Figure 10f reveals a film on the LNMO crystallite with a thickness of 24 nm. However, the micrograph of the electrode is shown to be complex in the case of ESS-30 with different solid phases mixed together, as seen in Figure 10b. The image in Figure 10c clearly displays the existence of two solid phases, which are demonstrated to be LNMO and Li_2SiO_3 by the corresponding EDX and electron diffraction patterns in Figure 10d and 10e,[25] respectively. Additionally, the film on the LNMO surface displays a thickness of ∼8 nm in the case of ESS-30 (Figure 10g), which is thinner than the one formed in the base electrolyte. Electrolyte reactions are partially suppressed in the presence of Li_2SiO_3. Additionally, the large amount of Li_2SiO_3 in the slurry electrolyte can retard the diffusion of organic species to reach to the cathode/electrolyte interface such that their accumulation on the interface is suppressed, which contributes to the thinner SEI film. The thinner film could decrease the electrode polarization with a small resistance, contributing to the performance enhancement of the cathode.

The scenario of the electrolyte/cathode interphase is illustrated schematically in Figure 11. In the case of the base carbonate electrolyte (Figure 11a), intensive electrolyte oxidation happens when cycled at high voltage, leading to a thick SEI film. Some HF exists in the electrolyte, originating from the hydrolysis of $LiPF_6$. This may accelerate Mn dissolution and also produce a lot of resistive LiF substance involved in the SEI film. However, in the case of the slurry electrolyte (Figure 11b), electrolyte oxidation is suppressed due to the high anodic stability, and a thinner SEI film is formed on the cathode surface. The stability of $LiPF_6$ is enhanced such that the contents of HF and PF_5 decrease. The conductivity of the lithium ion increases, as more Li^+ could take part in the charge transport. Moreover, the carbonate polymerization leading to electrolyte decay is also inhibited. Thus, fast lithiation/delithiation is achieved using the slurry electrolyte.

4. CONCLUSIONS

A novel slurry electrolyte with a large amount of insoluble inorganic Li_2SiO_3 is reported in this work. Compared to the base carbonate electrolyte, the slurry electrolyte possesses ∼27.5% shorter burning time, 35.4% higher Li^+ conductivity, and superior electrochemical and storage stability. It also brings about enhanced cyclic and rate performance of the 5 V LNMO electrode in the range of 3.5−5.0 V and 2.0−5.0 V. Between 2.0 and 5.0 V, the capacity of 173.8 mAh g^{-1} is still maintained after 120 cycles, whereas it is only 74.9 mAh g^{-1} with the base electrolyte. A capacity as high as 151.5 mAh g^{-1} can be delivered at 2 C, which is almost 2.5 times larger than that in the base electrolyte. All of these improvements are derived from three reasons. First, the anodic stability of the slurry electrolyte is enhanced, thus avoiding excess electrolyte oxidation. Second, $LiPF_6$ is stabilized in the presence of Li_2SiO_3, such that the decomposition of $LiPF_6$ is restricted. Third, the PF_5 produced is consumed by Li_2SiO_3. This work provides a novel electrolyte system in slurry state that proposes an effective approach to improving the electrochemical performance of high voltage cathodes.

AUTHOR INFORMATION

Corresponding Authors

*Tel./Fax: +86-10-68912657. E-mail: mudb@bit.edu.cn.
*E-mail: wubr2528@163.com.

Notes

The authors declare no competing financial interest.

ACKNOWLEDGMENTS

This project was financially supported by the National Natural Science Foundation and China Academy of Engineering Physics United Fund (NSAF, 11076003), the National 863 Program (2013AA050903) of China, Beijing Key Laboratory of Environmental Science and Engineering (20131039031), and Beijing Higher Institution Engineering Research Center for Power Battery and Chemical Energy Materials (2012039032).

REFERENCES

(1) Guo, Y. S.; Zhang, F.; Yang, J.; Wang, F. F.; NuLi, Y.; Hirano, S. Boron-based Electrolyte Solutions with Wide Electrochemical Windows for Rechargeable Magnesium Batteries. *Energy Environ. Sci.* **2012**, *5*, 9100−9106.

(2) Etacheri, V.; Marom, R.; Elazari, R.; Salitra, G.; Aurbach, D. Challenges in the Development of Advanced Li-ion Batteries: a Review. *Energy Environ. Sci.* **2011**, *4*, 3243−3262.

(3) Cho, J. H.; Park, J. H.; Lee, M. H.; Song, H. K.; Lee, S. Y. A Polymer Electrolyte-Skinned Active Material Strategy toward High-Voltage Lithium Ion Batteries: a Polyimide-Coated $LiNi_{0.5}Mn_{1.5}O_4$ Spinel Cathode Material Case. *Energy Environ. Sci.* **2012**, *5*, 7124−7131.

(4) Kraytsberg, A.; Ein-Eli, Y. Higher, Stronger, Better··· A Review of 5 V Cathode Materials for Advanced Lithium-Ion Batteries. *Adv. Energy Mater.* **2012**, *2*, 922−939.

DOI: 10.1021/acsami.5b05780
ACS Appl. Mater. Interfaces 2015, 7, 22898−22906

(5) Ariyoshi, K.; Iwakoshi, Y.; Nakayama, N. Topotactic Two-Phase Reactions of $Li[Ni_{1/2}Mn_{3/2}]O_4$ (P4(3)32) in Nonaqueous Lithium Cells. *J. Electrochem. Soc.* **2004**, *151*, A296−A303.
(6) Park, S.; Oh, S.; Kang, S. H.; Belharouak, I.; Amine, K.; Sun, Y. Comparative Study of Different Crystallographic Structure of $LiNi_{0.5}Mn_{1.5}O_{4-\delta}$ Cathodes with Wide Operation Voltage (2.0−5.0 V). *Electrochim. Acta* **2007**, *52*, 7226−7230.
(7) Yi, T. F.; Xie, Y.; Ye, M. F.; Jiang, L. J.; Zhu, R. S.; Zhu, Y. R. Recent Developments in the Doping of $LiNi_{0.5}Mn_{1.5}O_4$ Cathode Material for 5 V Lithium-ion Batteries. *Ionics* **2011**, *17*, 383−389.
(8) Song, J.; Shin, D. W.; Lu, Y. H.; Amos, C. D.; Manthiram, A.; Goodenough, J. B. Role of Oxygen Vacancies on the Performance of $Li[Ni_{0.5-x}Mn_{1.5+x}]O_4$(x = 0, 0.05, and 0.08) Spinel Cathodes for Lithium-Ion Batteries. *Chem. Mater.* **2012**, *24*, 3101−3109.
(9) Zhao, G. Y.; Lin, Y. B.; Zhou, T.; Lin, Y.; Huang, Y. D.; Huang, Z. G. Enhanced Rate and High-Temperature Performance of $La_{0.7}Sr_{0.3}MnO_3$-Coated $LiNi_{0.5}Mn_{1.5}O_4$ Cathode Materials for Lithium Ion Battery. *J. Power Sources* **2012**, *215*, 63−68.
(10) Fan, Y. K.; Wang, J. M.; Tang, Z.; He, W. C.; Zhang, J. Q. Effects of the Nanostructured SiO_2 Coating on the Performance of $LiNi_{0.5}Mn_{1.5}O_4$ Cathode Materials for High-Voltage Li-Ion Batteries. *Electrochim. Acta* **2007**, *52*, 3870−3875.
(11) Wang, H. L.; Xia, H.; Lai, M. O.; Lu, L. Enhancements of Rate Capability and Cyclic Performance of Spinel $LiNi_{0.5}Mn_{1.5}O_4$ by Trace Ru-Doping. *Electrochem. Commun.* **2009**, *11*, 1539−1542.
(12) Nagao, M.; Hayashi, A.; Tatsumisago, M. Fabrication of Favorable Interface between Sulfide Solid Electrolyte and Li Metal Electrode for Bulk-Type Solid-State Li/S Battery. *Electrochem. Commun.* **2012**, *22*, 177−180.
(13) Wu, B. R.; Ren, Y. H.; Mu, D. B.; Liu, X. J.; Wu, F. Modified Electrochemical Performance of High Potential Cathode Using a Sand-Like Carbonate Electrolyte. *Electrochim. Acta* **2014**, *143*, 324−330.
(14) Suo, L. M.; Hu, Y. S.; Li, H.; Armand, M.; Chen, L. Q. A New Class of Solvent-in-Salt Electrolyte for High-Energy Rechargeable Metallic Lithium Batteries. *Nat. Commun.* **2013**, *4*, 1481−1489.
(15) Bruce, P. G.; Vincent, C. A. Steady-State Current Flow in Solid Binary Electrolyte Cells. *J. Electroanal. Chem. Interfacial Electrochem.* **1987**, *225*, 1−17.
(16) Bruce, P. G.; Evans, J.; Vincent, C. A. Conductivity and Transference Number Measurement on Polymer Electrolytes. *Solid State Ionics* **1988**, *28*, 918−922.
(17) Evans, J.; Vincent, C. A.; Bruce, P. G. Electrochemical Measurement of Transference Numbers in Polymer Electrolytes. *Polymer* **1987**, *28*, 2324−2328.
(18) Tasaki, K.; Nakamura, S. Computer Simulation of $LiPF_6$ Salt Association in Li-Ion Battery Electrolyte in the Presence of an Anion Trapping Agent. *J. Electrochem. Soc.* **2001**, *148*, A984−A988.
(19) Sloop, S. E.; Pugh, J. K.; Wang, S.; Kerr, J. B.; Kinoshita, K. Chemical Reactivity of PF_5 and $LiPF_6$ in Ethylene Carbonate/Dimethyl Carbonate Solutions. *Electrochem. Solid-State Lett.* **2001**, *4*, A42−A44.
(20) Zhang, S. S. A Review on Electrolyte Additives for Lithium-Ion Batteries. *J. Power Sources* **2006**, *162*, 1379−1394.
(21) Sun, X.; Lee, H. S.; Yang, X. Q.; McBreen, J. Using a Boron-Based Anion Receptor Additive to Improve the Thermal Stability of $LiPF_6$-Based Electrolyte for Lithium Batteries. *Electrochem. Solid-State Lett.* **2002**, *5*, A248−A251.
(22) Lee, E. S.; Nam, K. W.; Hu, E. Y.; Manthiram, A. Influence of Cation Ordering and Lattice Distortion on the Charge-Discharge Behavior of $LiMn_{1.5}Ni_{0.5}O_4$ Spinel between 5.0 and 2.0 V. *Chem. Mater.* **2012**, *24*, 3610−3620.
(23) Sun, Y. K.; Oh, S. W.; Yoon, C. S.; Bang, H. J.; Prakash, J. Effect of Sulfur and Nickel Doping on Morphology and Electrochemical Performance of $LiNi_{0.5}Mn_{1.5}O_{4-x}S_x$ Spinel Material in 3-V Region. *J. Power Sources* **2006**, *161*, 19−26.
(24) Kang, S. H.; Goodenough, J. B. $Li[Mn_2]O_4$ Spinel Cathode Material Showing No Capacity Fading in the 3 V Range. *J. Electrochem. Soc.* **2000**, *147*, 3621−3627.
(25) Park, S. H.; Oh, S. W.; Yoon, C. S.; Myung, S. T.; Sun, Y. K. $LiNi_{0.5}Mn_{1.5}O_4$ Showing Reversible Phase Transition on 3 V Region. *Electrochem. Solid-State Lett.* **2005**, *8*, A163−A167.

DOI: 10.1021/acsami.5b05780
ACS Appl. Mater. Interfaces 2015, 7, 22898−22906